

Structure and conductivity characterization of new type ionic conductor stabilized bismuth oxide ternary systems

Serdar Yilmaz^{a,b,*}, Bekir Kavaci^b, Cigdem Celen^b, Esra Yildiz^c, Aynur Gurbuz^b

^a Mersin University, Physics Department, Mersin, Turkey

^b Mersin University, Nanotechnology and Advanced Materials Department, Mersin, Turkey

^c Bozok University, Yozgat, Turkey



ARTICLE INFO

Keywords:

X-ray diffraction
Conductivity characterization
Bismuth oxide
Electroceramics

ABSTRACT

In this study, the new type electrolyte $(Yb_2O_3)_x(Dy_2O_3)_y(Bi_2O_3)_{1-x-y}$ ternary compounds were synthesized with different stoichiometric ratios by the solid-state reaction method at different annealing treatment and also their microstructural and electrical properties were analysed. X-ray powder diffraction results showed that the high temperature δ -phase of pure monoclinic Bi_2O_3 has been synthesized by doping of Yb_2O_3 . Grain size and grain form of pellet formed samples was compared from their surface images taken by the scanning electron microscopy. The grain size has been varying between ~ 17 – $37 \mu m$, and degrading with the increasing dopant concentrations. The relationships between the structural parameters (e.g. lattice parameters, crystallite size and the lattice microstrain) and structural properties (e.g. ionic radii of dopant cations and heat treatment procedure) were particularly discussed. Total conductivity values were calculated by Nyquist complex impedance plot. Impedance measurement revealed that total conductivity values of the samples increase with the increasing Yb dopant ratio. The activation energies calculated by the Arrhenius approach are measured at around 1 eV. In addition, activation energies and pre-exponential terms decrease with the increasing Yb cation dopant rate for the same ambient temperature.

1. Introduction

Bi_2O_3 -based materials are used for the manufacturing of ceramic refractory, paint pigments, photovoltaic cells, oxygen sensors and oxygen pumps. Because of their higher ionic conductivity, Bi_2O_3 polymorphs show better solid electrolyte property than well-known zirconium oxide type electrolyte systems [1–7]. Zirconium based electroceramics that are used for solid oxide fuel cell applications have operating at temperatures up to 1000 °C today. In recent years, operating temperatures of zirconium-based electroceramics that are used for solid oxide fuel cell applications has been performed up to 1000 °C. Operating temperature of solid electrolyte based on bismuth oxide is lower than the ones based on zirconium. Bismuth oxide based electroceramics have oxygen ionic conductivity at about 600 °C and they are 5–15% more efficient than other electrolytes at these temperatures. Bismuth oxide has monoclinic (α) phase and transform to unstable cubic (δ) phase at about 730 °C [2]. These metastable phases could be stabilized at room temperature by doping with some lanthanide cations such as Dy^{3+} , Yb^{3+} , Ho^{3+} , Er^{3+} , Ta^{5+} , Y^{3+} [8–11]. Among the Bi_2O_3 -based solid electrolytes, the highest ionic-conductivity is observed at δ -phase (δ - Bi_2O_3) crystal structure which is attributed to the highly polarisable Bi^{3+} cations and highly disordered structure of sublattice [1,2,4–7]. Also, doped δ - Bi_2O_3 , γ - Bi_2O_3 and α - Bi_2O_3 phases have crystal defects which increase with increasing dopant rate and these defects are reported to result in O^{2-} ion deficiency

* Corresponding author.

E-mail addresses: syilmaz@mersin.edu.tr (S. Yilmaz), aynurgurbuz@mersin.edu.tr (A. Gurbuz).

<https://doi.org/10.1016/j.cjph.2017.11.010>

Received 26 July 2017; Received in revised form 16 November 2017; Accepted 17 November 2017

Available online 22 November 2017

0577-9073/ © 2017 The Physical Society of the Republic of China (Taiwan). Published by Elsevier B.V. All rights reserved.

[5,12].

In this study, we investigated the crystal structure and electrical conductivity properties of δ -YbDSB (*fcc*-phase stabilized with Yb_2O_3 and Dy_2O_3 doping) ternary systems. The effect of dopant ratio on the stabilization of δ -YbDSB was analysed. XRD Analysis, SEM and impedance measurement were performed to the samples for the physical characterizations.

2. Material and methods

2.1. Preparation of the sample

Firstly, $(\text{Yb}_2\text{O}_3)_x(\text{Dy}_2\text{O}_3)_y(\text{Bi}_2\text{O}_3)_{100-x-y}$ ternary systems (called by $x\text{YbyDSB}$) ($2 \leq x \leq 20$ mol% and $y = 10, 15, 20$ mol%) were synthesized by solid state reaction method. As starting materials, Yb_2O_3 (99.9% pure, Johnson Matthey, Royston, UK), Dy_2O_3 (99.9% pure, Johnson Matthey, Royston, UK) and Bi_2O_3 (99.99% pure, Johnson Matthey, Royston, UK) were used. Each mixed powder was ground in agate mortar for 10 min and annealed in alumina boat at 700, 750 and 800 °C temperature for 24 h, respectively. At the end of each heat treatment procedure, annealed powders were slowly cooled in the furnace and then were reground and characterized of microstructures.

2.2. Crystal structure analysis

XRD analysis (Rigaku Smartlab, Texas, USA) was performed to identifying of crystal structure and lattice parameters of synthesized powder materials. δ -phase powder ternary systems (δ -YbyDSB) were identified and also the study continued with these materials. The analysis conditions have been applied with these parameters; scanned by 0.02 step width, $7^\circ \leq 2\theta \leq 90^\circ$ angular range and 21.6746 °/min scanning speed in room temperature. The diffracted beams were counted with a 1D silicon strip detector (D/teX Ultra 250). XRD patterns were indexed and lattice parameter was calculated for each sample by PDXL2 software and DICVOL06 method [4].

The average crystallite size D was estimated according to the Williamson-Hall equation for each sample. The lattice strain in the crystallites was estimated by the single line method for analysis of X-ray diffraction line broadening using a pseudo-Voigt profile function [13]. The changing of the lattice parameters and crystallinity vs. dopant ratio were investigated. In this study, the effect of Yb_2O_3 addition on crystal structure was investigated when Dy_2O_3 dopant ratio was fixed.

2.3. Microstructure characterization

The δ -phase powders were ball milled by the planetary ball mill (Fritsch Pulverisette 6) at 500 rpm for 15 min in ethanol with agate ball media. After drying the grounded δ -phase 1.5 g powder materials were pressed into pellets with 0.16 cm thickness and ~1.3 cm diameter under 25 MPa pressure and sintered at 800 °C temperature for 24 h on a platinum substrate. Surface structure analyses of pellet samples were performed by SEM analysis (ZEISS SUPRA55, Oberkochen, Germany).

2.4. Conductivity measurements

Conductivities of pellets were calculated from impedance values. Impedance measurements was performed by two probe a.c. impedance analysis method using potentiostat/galvanostat system (Parstat 2273, Princeton Applied Research, Oak Ridge, TN, USA). Also, obtained data were analysed by the PowerSINE (Princeton Applied Research, Oak Ridge, TN, USA) software, over the frequency range between 10^{-1} Hz and 3×10^5 Hz and under the 50 mV potential. Silver platinum high conductivity paste (ESL, ElectroScience, Shanghai, China) was brushed onto both sides of the electrolytes and the organic additives were evaporated at 125 °C for 0.5 h. The conductivity measurements were performed from 400 °C to 800 °C. The heating rate was applied to 5 °C/min and holds for 10 min at each 50 °C steps for thermal stability. During the measurements, the sample temperature was determined by a thermocouple, 5 mm away from the sample. Equivalent circuit analysis was used ZSimpWin (Princeton Applied Research, Oak Ridge, TN, USA) software.

The resistances were read from real axis of the Nyquist impedance plots. Total resistance (R) is sum of the grain bulk (R_b) and grain boundary (R_{gb}) resistances (Eq. (1)).

$$R = R_b + R_{gb} \quad (1)$$

The total ionic conductivities (σ) for the sample were calculated from Eq. (2). Where, t thickness of sample and S current collector area contact with the sample (electrode).

$$\sigma = \frac{1}{R} \frac{t}{S} \quad (2)$$

The ionic conductivity can be explained as an exponential function of the activation energy for oxygen vacancy diffusion (Eq. (3)). The activation energies and pre-exponential factors were calculated using the Eq. (3).

$$\sigma = \sigma_0 e^{-E_a/k_b T} \quad (3)$$

In Eq. (3), σ_0 , E_a , k_b and T is the pre-exponential factor, total activation energy for the ionic conduction via oxygen vacancy diffusion, Boltzmann constant and absolute temperature, respectively.

3. Result and discussion

3.1. Microstructure analysis

Observed phases, synthesizing temperatures and times of $(\text{Yb}_2\text{O}_3)_x(\text{Dy}_2\text{O}_3)_y(\text{Bi}_2\text{O}_3)_{100-x-y}$ ternary systems are seen in Table 1. In $(\text{Yb}_2\text{O}_3)_x(\text{Dy}_2\text{O}_3)_y(\text{Bi}_2\text{O}_3)_{1-x-y}$ ternary systems, the *fcc* cubic phases (δ -phase) were observed at low total dopant ratio. The δ -*fcc* phase was not observed at 700 °C heat treated samples. Numbers of observed δ -*fcc* phases were increased with increasing temperature. Also, the number of transformed to poly-phases ($\delta + \alpha$ -phases) from single δ -*fcc* phase increased with increasing total dopant ratio.

The XRD patterns of $x\text{Yb}10\text{DSB}$ samples which were sintered at 800 °C for 24 h are shown in Fig. 4a. The *hkl* values of the *fcc*-crystal structure are indicated on the peaks. $x\text{Yb}10\text{DSB}$ systems for $x = 8, 10, 12$ and 14 mol% have single *fcc* crystal phase (δ -phase). In Fig. 4b, the magnified version of $2\theta = 25^\circ\text{--}32^\circ$ of XRD patterns are given. As can be seen in this figure, the peaks of monoclinic α -phase were observed together with *fcc* in the 16Yb10DSB, 18Yb10DSB and 20Yb10DSB samples. As the amount of dopant increased, the intensity of monoclinic α -phase peaks increased. This shows that the amount of crystals with monoclinic α -phase increased. The XRD patterns of the $x\text{Yb}15\text{DSB}$ samples for $x = 8, 10, 12, 14, 15$ and 20 mol% which were heated at 800 °C for 24 h are shown in Fig. 5a. Only 8Yb15DSB and 10Yb15DSB have *fcc* single crystal phase. Also in here, the peaks of monoclinic α -phase of 12Yb15DSB, 14Yb15DSB, 15Yb15DSB and 20Yb15DSB samples are shown. As the ratio of total dopant decreased, the peak intensities of monoclinic α -phase decreased and the transition to *fcc* structure occurred with the sample of 10Yb15DSB. XRD patterns of $x\text{Yb}20\text{DSB}$ ($x = 2, 4, 6, 8, 10, 15$ and 20 mol%) annealed 24 h at 800 °C are seen in Fig. 6a. 2Yb20DSB, 4Yb20DSB and 6Yb20DSB samples are *fcc*-phase as seen in this figure. The magnified version of $2\theta = 25^\circ\text{--}32^\circ$ XRD patterns of the other 8Yb20DSB, 10Yb20DSB, 12Yb20DSB and 14Yb20DSB samples in the heterogeneous crystal phase are shown in Fig. 6b. Also in here, the monoclinic α -phase peak intensities decreased as the dopant ratio decreased. With the sample of 6Yb20DSB, the monoclinic α -crystal phase completely disappeared and *fcc* homogeneous crystal phase samples were observed.

As seen in phase distribution map (Fig. 1), 10 mol% Dy_2O_3 doped and also 14 mol% and less Yb_2O_3 doped systems have *fcc* crystal structure and however higher than 14 mol% Yb_2O_3 doping have mixing of *fcc* and monoclinic crystal structure for $x\text{Yb}10\text{DSB}$ systems. Also, it was observed that $x\text{Yb}15\text{DSB}$ systems for $x = 8$ and 10 mol% have *fcc* crystal structure but on the other hand these systems were mixed *fcc* and monoclinic phases for x value higher than 10 mol%. $x\text{Yb}20\text{DSB}$ samples have *fcc* crystal structure for $x = 2, 4$ and 6 mol% but for higher than 6 mol% Yb_2O_3 doping the systems have mixed *fcc* and monoclinic crystal structure. According to this result, Yb_2O_3 dopant rate should be decreased while Dy_2O_3 has been increasing and total doping amount should be constant at a certain ratio to obtain *fcc*-phases. It was observed that maximum x mol% dopant ratio with single *fcc* crystal structure (δ -phase) was 24 mol% for $x\text{Yb}10\text{DSB}$ systems, 25 mol% for $x\text{Yb}15\text{DSB}$ systems and 26 mol% for $x\text{Yb}20\text{DSB}$ systems. Also, opposite of this state heterogeneous crystal structure occurs while *fcc* crystal structure damaged. The total contribution ratio increases distorted cubic structure [5].

Lattice parameter values related with total dopant concentration is shown in Fig. 2 for single δ -phase $x\text{Yb}10\text{DSB}$ samples ($x = 8, 10, 12, 14$ mol%). Numerical values were also given in Table 2. While amount of Yb_2O_3 increases, lattice parameter decreases orderly. This lattice parameter changing is in good agreement with the effective ionic radii considerations. The Dy and Yb cations have smaller ionic radii than Bi^{3+} cation in lattice (for six-coordinated O^{2-} 1.40 Å, Bi^{3+} 1.030 Å, Dy^{3+} 0.912 Å, Yb^{3+} 0.868 Å and Yb^{2+} 1.02 Å, Dy^{2+} 1.07 Å and Yb^{2+} 1.02 Å) [14]. Accordingly, as the contribution Dy_2O_3 and/or Yb_2O_3 increases within δ - Bi_2O_3 , the settlement of dopant cations with lower ionic radii within crystal lattice points cause a regular decrease in unit cell constants.

Crystal imperfections and deviations from perfect crystallinity lead to broadening of the diffraction peaks in the XRD pattern. The strain and crystallinity can be commented by the analysis of this peak broadening. The microstructural effects responsible for the peak broadening are the crystallite size distribution and the lattice microstrain within the crystallites introduced due to lattice defects

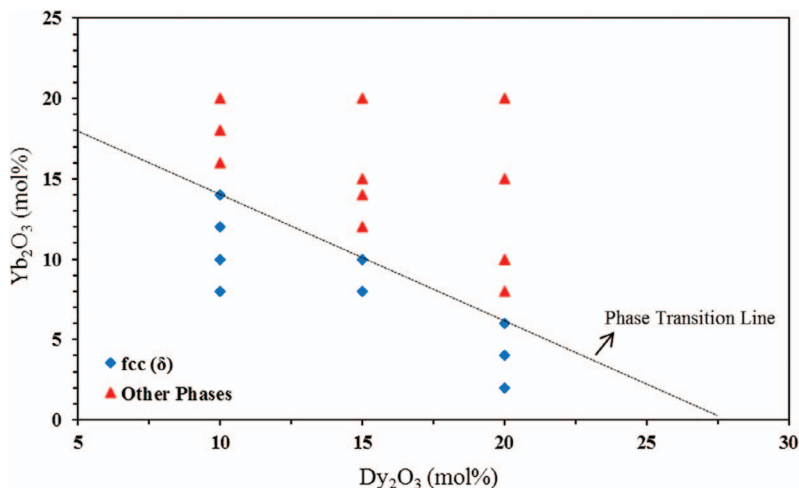


Fig. 1. The phase distribution of powder samples annealed 24 h at 800 °C.

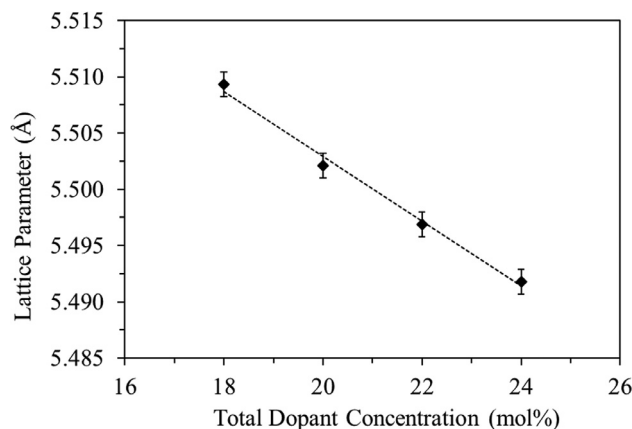


Fig. 2. Lattice parameters changing of 10 mol% Dy₂O₃ ternary systems as a function of total dopant concentration annealed 24 h at 800 °C.

Table 2

Lattice parameters, crystalline size and lattice strain of δ -YbDSB system.

Samples (δ -phases)	Lattice parameter (Å)	Crystallite size (Å)	Lattice strain (%)
8Yb10DSB	5.5093	987	0.045
10Yb10DSB	5.5021	1192	0.099
12Yb10DSB	5.4969	1497	0.167
14Yb10DSB	5.4918	1824	0.220

[15]. Lattice strain and microstrain are close in meaning [16]. But on the other hand, the isotropic nature and having point defects of ceramic crystals such as the ZrO₂ is suggested presuming that, the strain is uniform in different directions, not one direction, and this statement leading to independent crystal properties [17]. So in here, it is more accurate that using *microstrain* term for local distortions of lattice planes and other microstructural effects such as the point defects. Williamson-Hall method takes crystallite size and lattice microstrain effects into account as the two biggest factors affect peak width. According to this method, the sum of these two factors are associated with peak broadening.

$$D = \frac{K\lambda}{\beta_{hkl} \cos \theta_{hkl}} \quad (4)$$

$$\varepsilon = \frac{\beta_{hkl}}{4 \tan \theta_{hkl}} \quad (5)$$

The Eq. (4) is known as Scherrer equation and gives us information about crystallinity and the Eq. (5) is known as Stokes-Wilson equation and is gives to us microstrain (ε). In these equations, D is the average crystallite size (in nm) measured in a direction perpendicular to the surface of the sample and ε is the microstrain in lattice induced in powders due to crystal imperfection and distortion. And also, K is the constant shape factor ($K = 0.9$ for small cubic crystal), λ is the wavelength of the X-rays ($\lambda = 0.154056$ nm for CuK α_1 radiation), β_{hkl} is the hkl diffraction peak width measured at half of its maximum intensity and θ_{hkl} is the half of the diffraction peak position (2θ) in radians. θ_{hkl} is the half of the diffraction peak position (2θ) in radians. When the Scherrer's particle effect and the Stokes-Wilson's microstrain effect is combined, the Williamson-Hall's equation for the β_{hkl} peak width analysis (Eq. 6).

$$\beta_{hkl} = \frac{K\lambda}{D \cos \theta} + (4 \tan \theta) \varepsilon \quad (6)$$

Williamson-Hall equation (Eq. (6)) is similar to linear equation in terms of $y = a + bx$. Therefore, the slope of this equation gives the effect on β_{hkl} peak width of lattice microstrain and crystallite size.

The changes in total dopant concentration versus crystallite size and microstrain of δ -phase xYb10DSB samples for $x = 8, 10, 12, 14$ mol% are shown in Fig. 3. The crystallite size and microstrain increase steadily as the dopant ratio increases (Fig. 3). Microstrain is a condition related to atomic (Oxygen) vacancy. Cubic structure (δ -phase) is high temperature polymorph of pure bismuth oxide [2]. It's crystal structure has lattice defect which is originated from two Oxygen ions vacancy in sublattice [5,18]. This unstable δ -phase can be stable via doping regime of Lanthanide group elements in pure bismuth oxide. Dopant cations replace with the host Bi³⁺ cations during the doping. During this substitution reaction, ionic radii difference of dopant and bismuth cations cause the remove of more oxygen ions from sublattice. In this case, the number of crystal structure which have oxygen ion defect in lattice in other words the atomic vacancy increases with the increasing dopant rate. According to this, the oxygen vacancy increase with the increasing dopant rate [11,19]. The increase in atomic vacancies in the crystal causes the lattice strain and also the microstrain rate increases. In

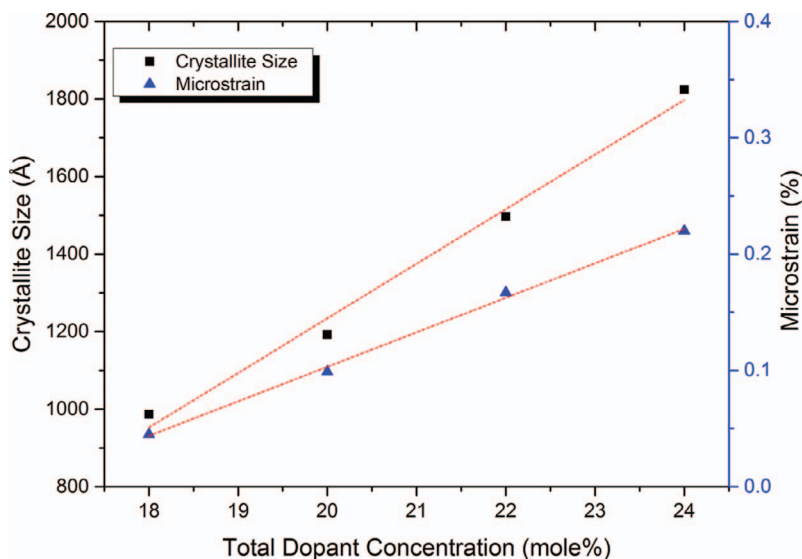


Fig. 3. Crystallite size and lattice strain changing of 10 mol% Dy_2O_3 ternary systems as a function of total dopant concentration annealed 24 h at 800 °C.

the XRD patterns, $\text{CuK}\beta$ (Figs. 4b, 5b, 6b) emission peaks were also observed. However, the peaks of $\text{CuK}\alpha_1$ ($\lambda = 1.54056 \text{ \AA}$) were used in indexing.

SEM micrograph of sintered film at 800 °C for 24 h of $x\text{Yb}10\text{DSB}$ systems is seen in Fig. 7. The micrograph has fine-spherical grains varying between $\sim 17\text{--}37 \mu\text{m}$ and degrades with the dopant concentration increases. The grain size distribution was not homogeneous at the low total doping concentration and conversely at high total dopant concentration level grain size distribution was more homogeneous.

3.2. Conductivity characterization

Total conductivity values of $x\text{Yb}10\text{DSB}$ ($x = 8, 10, 12$ and 14 mol%) ternary systems (σ) were calculated from total bulk resistance values (R) removed from low and high intercepts of complex impedance plots. Fig. 8 typical impedance plots of $x\text{Yb}10\text{DSB}$ ($x = 8, 10, 12$ and 14 mol%) samples at 800 °C. In these Nyquist Plots, the slopes are seen in depressed semi-circular form. In practices the semicircles have small depressed form like as semi-circular arcs as seen in Fig. 8. These small depressions of the grain boundary and electrode semicircle indicates a small scatter of relaxation times [20,21] and can be correlated with homogeneous grain boundaries [22]. A large depression angle is also observed for sodium beta aluminas [20] and this material shows conduction anisotropy and a

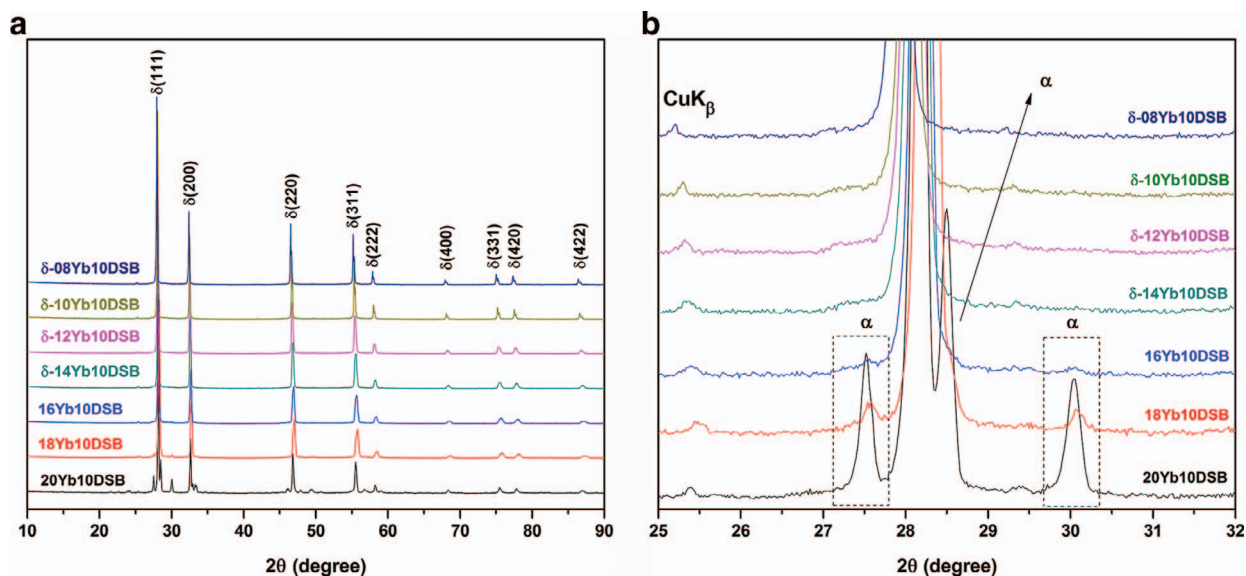


Fig. 4. $x\text{Yb}10\text{DSB}$ ($x = 8, 10, 12, 14, 16, 18$ and 20 mol%) annealed 24 h at 800 °C (a) XRD patterns and (b) magnified version of $2\theta = 25^\circ\text{--}32^\circ$.

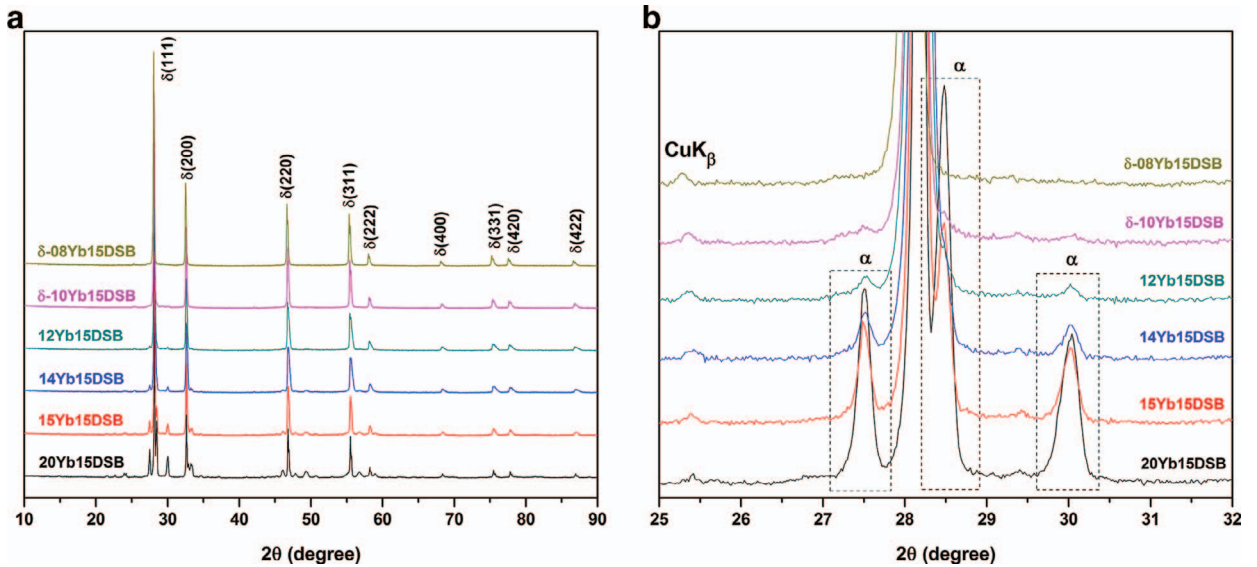


Fig. 5. $x\text{Yb}15\text{DSB}$ ($x = 8, 10, 12, 14, 15$ and 20 mol%) annealed 24 h at 800 °C (a) XRD patterns and (b) magnified version of $2\theta = 25^\circ\text{--}32^\circ$.

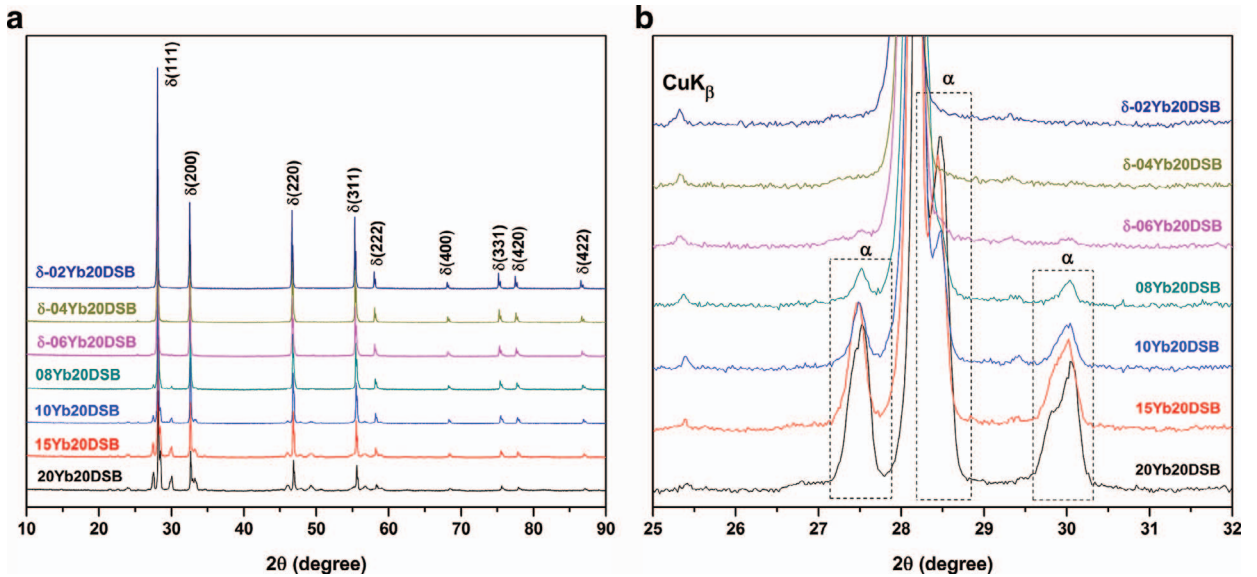


Fig. 6. $x\text{Yb}20\text{DSB}$ ($x = 2, 4, 6, 8, 10, 15$ and 20 mol%) annealed 24 h at 800 °C (a) XRD patterns and (b) magnified version of $2\theta = 25^\circ\text{--}32^\circ$.

large scatter of relaxation times can be expected [22]. Charge transfer polarization, however, gives rise to a much larger depression of the characteristic semi-circular arc below the real axis [21]. Also, the deformed semicircle and also the non-ideal capacitor behaviour for the solid electrolytes like as double layer capacitance C_{dl} of constant phase element CPE and electrodes may result from surface inhomogeneity [23] like as irregular thickness, morphology of sample and roughness of the electrode surface [24]. On the other hands, the influence of grain boundaries on conductivity varies depending on temperature [25]. Therefore, the complex impedance plot (number and size of semicircles) may also vary with temperatures [26].

A typical Nyquist complex impedance plot of a solid electrolyte has three semicircles [27]. As seen in Fig. 9, the intercepts with the real axis will be referred to as bulk of grain, grain boundary and electrode resistances denoted with R_b , R_{gb} and R_e respectively. These semicircles, the first from left semicircle at the high-frequency region (numbered 1) is assigned to the grain bulk resistance (R_b) and at the medium frequency region semicircles (numbered 2) corresponds to the grain boundary contribution (R_{gb}) [28]. The R_{gb} semicircle often appears in middle frequency region for Oxygen ionic conductors such as stabilized zirconia [29] and bismuth oxides [30]. Also, the low frequency region (numbered 3) can be explained by electrode resistance (R_e) [22,29]. The low frequency semicircle is usually attributed to the blocking of charge carriers at electrolyte-electrode interfaces [30]. There is no full circular arc associated with the electrode resistance at low frequency region in impedance plots because of the limited frequency range of the galvanostat system (minimum value of 0.1 Hz) and not be separated from electrode arc and is consolidated in to a highly-depressed

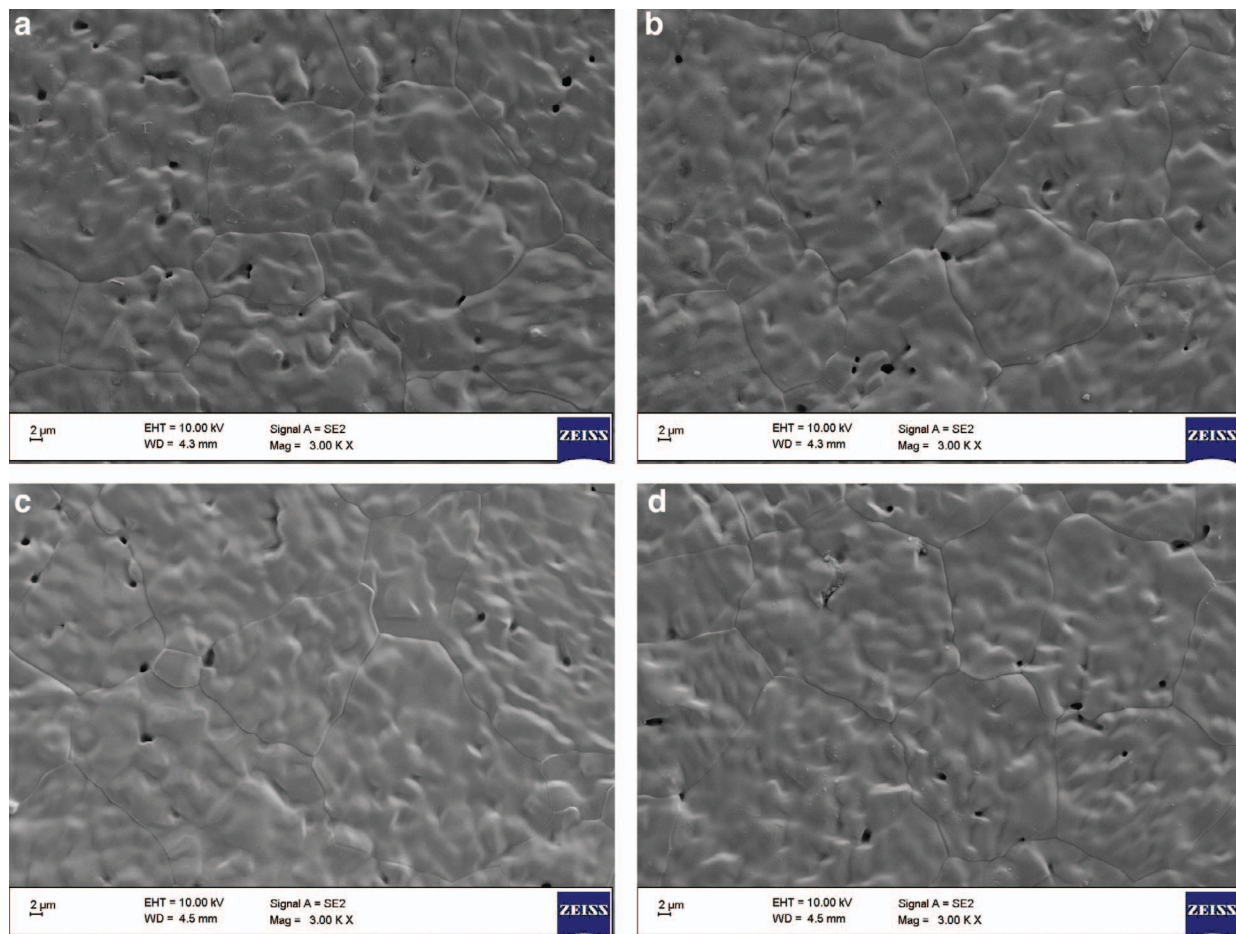


Fig. 7. SEM micrographs of sintered disc at 800 °C for 24 h of (a) 8Yb10DSB and (b) 10Yb10DSB (c) 12Yb10DSB and (d) 14Yb10DSB.

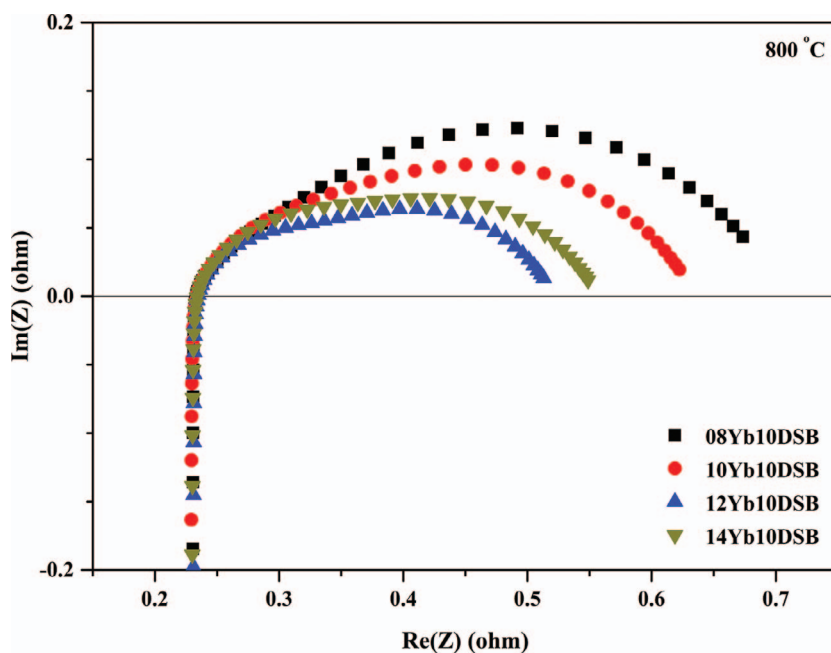


Fig. 8. Complex impedance plots of xYb10DSB (x = 8, 10, 12 and 14 mol%) at 800 °C.

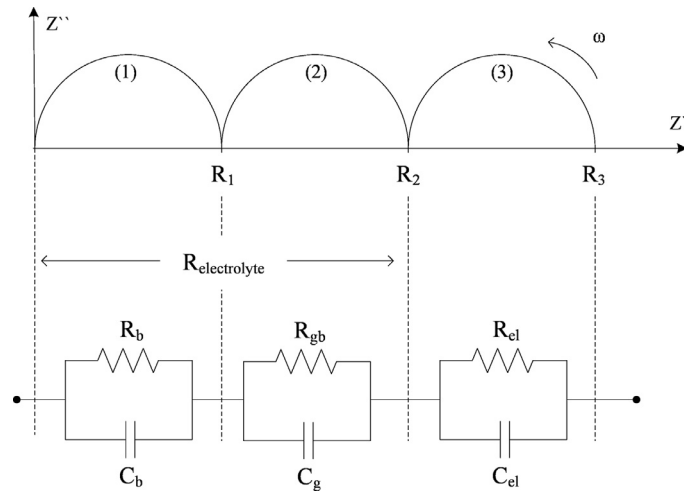


Fig. 9. The equivalent circuit of complex impedance plot sample with three semicircles.

semicircle. Also, the circular arc of the grain boundary resistance in the middle frequency regions was seen as depressed semi-circular too. The circular arc of bulk resistance R_b could not have been observed in plot because of the samples exhibit pure resistance behaviour as seen in Figs. 9 and 10.

The impedance plot of 12Yb10DSB is seen in Fig. 10. The electrical conductivity can be calculated from the interception of the depressed circular arcs on the real axis. From the complex impedance plot, the total conductivities each of the electrolyte was calculated from Eq. (2). In Eq. (1), sum of the bulk resistance (R_b) and the grain boundary resistance (R_{gb}) gives the total resistance (R). The R_b read as R_1 from Fig. 10 and also R_{gb} read as difference between R_2 and R_1 from Fig. 10. Fig. 10 and Eq. (7) evaluated together, it is seen that the total resistance R is equal to R_2 .

$$\left. \begin{matrix} R_b = R_1 \\ R_{gb} = R_2 - R_1 \end{matrix} \right\} \rightarrow R = R_2 \tag{7}$$

Also, the supposed equivalent circuit of 12Yb10DSB is seen in Fig. 11. In supposed equivalent circuit, the inductance at very high frequency region was attributed to artefact arising from the device and silver current collector and silver wires as explained by Mauvy et al. [28]. The high frequency semicircle (first from left) represented the bulk resistance of the inside of the grains, the intermediate frequency semicircle provides the grain boundary resistance and capacitance and the low frequency semicircle provides the information on the oxygen-ion transfer at the electrodes. Table 3 shows calculated total conductivities of disc samples x Yb10DSB ($x = 8, 10, 12$ and 14 mol%) sintered 24 h at various temperatures and also the dimensions of under the test pellet samples.

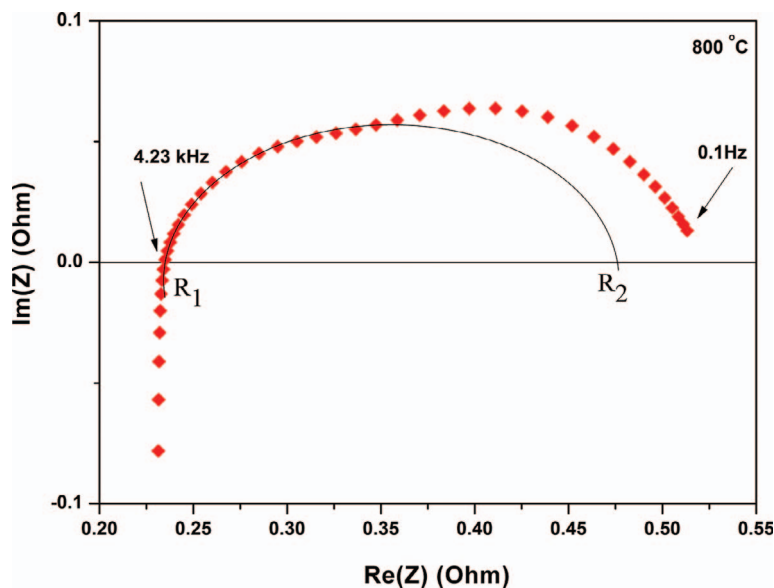


Fig. 10. Impedance spectra of 12Yb10DSB at 800 °C.

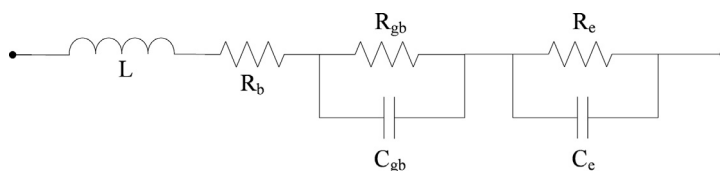


Fig. 11. Equivalent circuit of 12Yb10DSB impedance spectra at 800 °C.

Table 3

Resistivities and conductivities of xYb10DSB (x = 8, 10, 12 and 14 mol%) sintered 24 h at 800 °C.

	T (°C)	8Yb10DSB	10Yb10DSB	12Yb10DSB	14Yb10DSB
$\sigma_{tot.} (\text{Scm}^{-1})$	800	0.3107	0.3904	0.5084	0.5185
	750	0.3051	0.3891	0.4107	0.4288
	700	0.1803	0.1495	0.1480	0.1462
	650	0.0569	0.0585	0.0657	0.0650
	600	0.0315	0.0374	0.0437	0.0397
	550	0.0195	0.0213	0.0259	0.0202
	500	0.0114	0.0097	0.0083	0.0068
	450	0.0042	0.0035	0.0037	0.0044
	400	0.0009	0.0012	0.0015	0.0017
	Geometry	t (cm)	0.16	0.16	0.16
d (cm)		1.21	1.16	1.18	1.13
S (cm ²)		1.15	1.05	1.09	1.01
E_a (eV)		0.95	0.93	0.92	0.90
σ_0		13737.7	10835.7	10317.5	6978.6

Consequently, as seen in Fig. 9 and Table 3, 08Yb10DSB sample has highly total resistance and also minimum total conductivity value among all of the other samples. The atomic vacancies in stabilized bismuth exhibit ionic conductivity and the lattice defect and also ionic conductivity increase with the increasing the dopant concentration [18]. The conductivity increase as the ratio of the Yb dopant increases. Also the temperature increased, the conductivity increased as normally.

Total activation energy (E_a) is calculated by following equation [31,32].

$$E_a = E_m + E_d \quad (8)$$

E_m is the migration activation energy for jumping interstitial O^{2-} ions to the correct O^{2-} vacancy positions and E_d is the additional energy required to break up the defect associates. As a general rule, E_d shows a decrease with the increasing ionic radii of the dopant cation [31,32]. E_a is directly related to the mobility (μ) of the oxygen ions which is dominated by the following Nernst–Einstein equation (Eq. (9)) [19,31–33].

$$\mu = \frac{q}{k_b T} D = \frac{Ze}{k_b T} [D_0 \exp(-E_a/k_b T)] \quad (9)$$

In Eq. (9), D is the O^{2-} diffusion coefficient and it changes exponentially with the temperature. Also in Eq. (9), q is equal to the multiplication of atomic number and the elementary electric charge (Ze) for the ionic conductors [34].

$$\sigma_i = Ze\mu = \left(\frac{nZ^2 e^2 D_0}{k_b T} \right) \exp(-E_a/k_b T) = \sigma_0 \exp(-E_a/k_b T) \quad (10)$$

The graphics of the changing of conductivity data versus temperature were fitted according to the Eq. (3) for the obtain of E_a (Fig. 12). As seen the plots in Fig. 12, behaviour of the conductivity changing is the Arrhenius type for all the samples. The calculated activation energy and pre-exponential factor data were given in Table 3. As seen in Table 3, energy values showed change depend on dopant rate and exhibited about 1 eV. Activation energies of the bismuth-based stabilized solid electrolytes have always exhibit about 1 eV in literature [34–37]. The activation energies decrease when the Yb cation dopant rate increasing for the same ambient temperature. Also as seen in Eq. (10), pre-exponential term point to diffusion and mobility parameters. The pre-exponential terms decrease when the Yb cation dopant rate increasing for the same ambient temperature.

4. Conclusion

The high temperature stable δ -phase of Bi_2O_3 polymorph have been obtained by doping of Yb_2O_3 into the pure monoclinic δ - Bi_2O_3 via solid state reaction method. Because of the ionic radii values of dopant and Bismuth atoms, the lattice parameter was decrease with the increasing dopant ratio. Conversely, the crystallite size and lattice strain was increase with increasing dopant rate. The conditions required for production the cubic phase materials have been determined. Only when total dopant ratio was ~ 25 mol% and below, the cubic phases was obtained. Also, the temperature required for synthesis of δ -phases was estimated as 750 °C and above. At the sintered temperature 800 °C and 12 h was enough for δ -phases synthesis. After the heat treatment of pellet samples

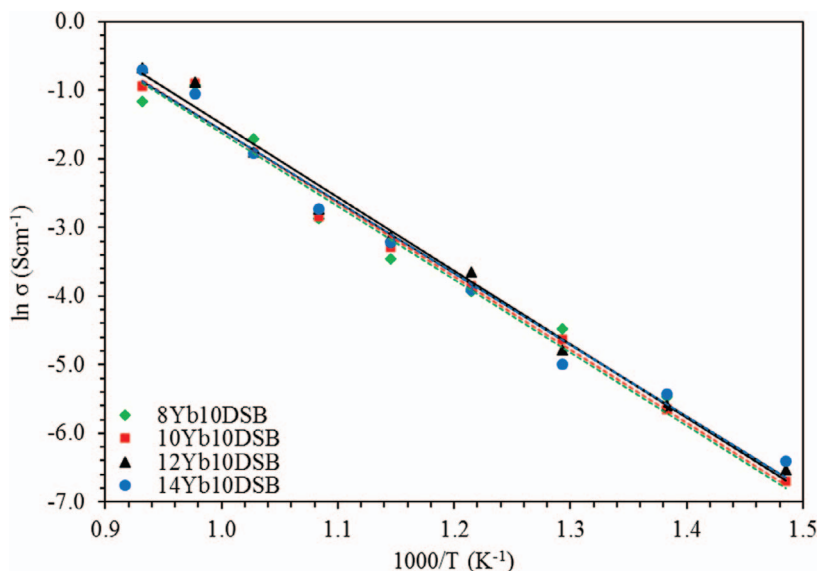


Fig. 12. Arrhenius plot of conductivities xYb10DSB ($x = 8, 10, 12$ and 14 mol%) sintered 24 h at 800 °C.

grain formations were observed.

Resistances of δ -phases read from Nyquistic Plots by Electrochemical Impedance Analysis. Conductivities were calculated from the total resistances using sample geometrical properties. The highest conductivity was obtained as 0.508 Scm^{-1} for 12Y10DSB sample at 800 °C. It has been determined that the conductivity is affected positively by the increase of the dopant amount. The conductivity behaviours were Arrhenius type. So, the activation energies were calculated from conductivity versus temperature plots. On the other hand, activation energies were decrease with increasing total dopant ratio and the highest value were obtained 0.9 eV .

Acknowledgements

The author would like thanks to Mersin University for their support (Grant No. FBE FB (BK) 2014-1 YL).

Supplementary materials

Supplementary material associated with this article can be found, in the online version, at [doi:10.1016/j.cjph.2017.11.010](https://doi.org/10.1016/j.cjph.2017.11.010).

References

- [1] T. Takahashi, H. Iwahara, Y. Nagai, High oxide ion conduction in sintered bismuth oxide containing strontium oxide, calcium oxide or lanthanum oxide, *J. Appl. Electrochem.* 2 (1972) 97–104.
- [2] H.A. Harwig, On the structure of Bismuthsesquioxide: the α , γ and δ -phase, *Z. Anorg. Allg. Chem.* 444 (1978) 151–166.
- [3] E.D. Wachsman, S. Boyapati, M.J. Kaufman, et al., Modeling of ordered structures of phase-stabilized cubic Bismuth Oxides, *J. Am. Ceram. Soc.* 83 (2000) 1964–1968.
- [4] A. Boulouf, D. Louer, Powder pattern indexing with the Dichotomy method, *J. Appl. Cryst.* 37 (2004) 724–731.
- [5] N.M. Sammes, G.A. Tompeest, H. Nafe, et al., Bismuth based oxide electrolytes-structure and ionic conductivity, *J. Eur. Ceram. Soc.* 19 (1999) 1801–1826.
- [6] T. Takahashi, H. Iwahara, Y. Nagai, High oxide ion conduction in sintered Bi_2O_3 containing SrO, CaO or La_2O_3 , *J. Appl. Electrochem.* 2 (1972) 97–104.
- [7] S. Nakayama, Electrical properties of $(\text{Bi}_2\text{O}_3)_{0.75}(\text{RE}_2\text{O}_3)_{0.25}$ ceramics (RE = Dy, Y, Ho, Er and Yb), *Ceram. Int.* 28 (2002) 907–910.
- [8] E.D. Wachsman, S. Boyapati, N. Jiang, Effect of dopant polarizability on Oxygen sublattice order in phase-stabilized cubic Bismuth Oxides, *Ionics* 7 (2001) 1–6.
- [9] S.E. Lin, W.C.J. Wei, Long-term degradation of Ta_2O_5 -doped Bi_2O_3 systems, *J. Am. Ceram. Soc.* 31 (2011) 3081–3086.
- [10] S. Bandyopadhyay, A. Dutta, Microstructure and charge carrier dynamics in Dy substituted phase stabilized cubic Bi_2O_3 , *RSC Adv.* 65 (2015) 65123–65132.
- [11] E. Ersoy, S. Çakar, E. Yıldız, et al., Fabrication and characterization of Dysprosium doped Bismuth Oxide films for IT-SOFCs via slurry spin coating technique, *Int. J. Appl. Ceram. Technol.* 12 (2015) 152–161.
- [12] H.A. Harwig, A.G. Gerards, Electrical properties of the α , γ and δ phases of Bismuth Sesquioxide, *J. Solid State Chem.* 26 (1978) 265–274.
- [13] A. Guinier, X-ray Diffraction in Crystals, Imperfect Crystals, and Amorphous Bodies, W. H. Freeman and Company, San Francisco, 1963.
- [14] R.D. Shannon, Revised effective ionic radii and systematic studies of interatomic distances in halides and chalcogenides, *Acta Cryst. A.* 32 (1976) 751–767.
- [15] R. Krishna, J. Wade, A.N. Jones, M. Lasithiotakis, P.M. Mummery, B.J. Marsden, An understanding of lattice strain, defects and disorder in nuclear graphite, *Carbon* 124 (2017) 314–333.
- [16] E.J. Mittemeijer, U. Welzel, The “state of the art” of the diffraction analysis of crystallite size and lattice strain, *Z. Kristallogr.* 223 (2008) 552–560.
- [17] K.A. Aly, N.M. Khalil, Y. Algamal, Q.M.A. Saleem, Estimation of lattice strain for zirconia nano-particles based on Williamson–Hall analysis, *Mat. Chem. Phys.* 193 (2017) 182–188.
- [18] S. Boyapati, E.D. Wachsman, N. Jiang, Effect of oxygen sublattice ordering on interstitial transport mechanism and conductivity activation energies in phase-stabilized cubic bismuth oxides, *Solid State Ionics* 140 (2001) 149–160.
- [19] M.J. Verkerk, A.J. Burggraaf, High Oxygen ion conduction in sintered oxides of the Bi_2O_3 - Ln_2O_3 system, *Solid State Ionics* 3/4 (1981) 463–467.
- [20] L.C. De Jonghe, Grain boundaries and ionic conduction in Sodium beta Alumina, *J. Mater. Sci.* 14 (1979) 33–48.
- [21] H.J. Bruin, A.D. Franklin, An impedance spectroscopy model for electron transfer reactions at an electrode/solid electrolyte interface, *J. Electroanal. Chem.* 118

- (1981) 405–418.
- [22] M.J. Verkerk, B.J. Middelhuis, A.J. Burggraaf, Effect of grain boundaries on the conductivity of high-purity $\text{ZrO}_2\text{-Y}_2\text{O}_3$ ceramics, *Solid State Ionics* 6 (2) (1982) 159–170.
- [23] G.J. Brug, A.L.G. van den Eeden, M. Sluyters-Rehbach, J.H. Sluyters, The analysis of electrode impedances complicated by the presence of a constant phase element, *J. Electroanal. Chem.* 176 (1984) 275–295.
- [24] X. Qian, N. Gu, Z. Cheng, et al., Methods to study the ionic conductivity of polymeric electrolytes using a.c. impedance spectroscopy, *J. Solid State Electrochem.* 6 (2001) 8–15.
- [25] N.Q. Minh, T. Takahashi, *Science and Technology of Ceramic Fuel Cells*, Elsevier, Amsterdam, 1995.
- [26] P. Timakul, S. Jinawath, P. Aungkavattana, Fabrication of electrolyte materials for solid oxide fuel cells by tape-casting, *Ceram. Int.* 34 (4) (2008) 867–871.
- [27] J.E. Bauerle, Study of solid electrolyte polarization by a complex admittance method, *J. Chem. Phys. Solids* 30 (1969) 2657–2670.
- [28] F. Mauvy, J.M. Bassat, E. Boehm, Oxygen electrode reaction on $\text{Nd}_2\text{NiO}_{4+8}$ cathode materials: impedance spectroscopy study, *Solid State Ionics* 158 (2003) 17–28.
- [29] T. Dijk, A.J. Burggraaf, Grain boundary effects on ionic conductivity in ceramic $\text{Gd}_x\text{Zr}_{1-x}\text{O}_{2-(x/2)}$ solid solutions, *Phys. Status Solidi A.* 63 (14) (1981) 229–240.
- [30] S. Beg, S. Haneef, N.A.S. Al-Areqi, Study of electrical conductivity and phase transition in $\text{Bi}_2\text{O}_3\text{-V}_2\text{O}_5$ system, *Phase Transitions* 83 (12) (2010) 1114–1125.
- [31] R. West, *Basic Solid State Chemistry*, John Wiley & Sons, Chichester, 1988.
- [32] C. Kittel, *Introduction to Solid State Physics*, John Wiley & Sons, New York, 2005.
- [33] J.B. Goodenough, Ceramic solid electrolytes, *Solid State Ionics* 94 (1997) 17–25.
- [34] S. Yilmaz, Synthesis Characterization and Investigation of the Solid State Oxygen Ionic Conductivities of $\beta\text{-Bi}_2\text{O}_3$ Type Solid Electrolytes Doped with Dy_2O_3 , Eu_2O_3 , Sm_2O_3 , Ph.D. Thesis, Gazi University, Ankara, 2008.
- [35] N. Ozpozan Kalaycıoğlu, E. Öztürk, S. Dayan, Oxide ionic conductivity properties of binary $\delta\text{-(Bi}_2\text{O}_3)_{1-x}(\text{Yb}_2\text{O}_3)_x$ system, *J. Chin. Adv. Mater. Soc.* 1 (1) (2013) 74–80.
- [36] T. Tunç, İ. Uslu, Ş. Durmuşoğlu, S. Keskin, A. Aytimur, A. Akdemir, Preparation of Gadolinia stabilized Bismuth Oxide doped with Boron via electrospinning technique, *J. Inorg. Organomet. Polym.* 22 (2012) 105–111.
- [37] M. Ari, İ. Taşcıoğlu, Ş. Altındal, İ. Uslu, A. Aytimur, T. Karaaslan, S. Koçyiğit, Crystal structure and electrical properties of Gadolinia doped Bismuth Oxide nanoceramic powders, *Mater. Chem. Phys.* 136 (2012) 942–946.